

Identifying Quantum Phase Transitions with Minimal Prior Knowledge by Unsupervised Learning

Mohamad Ali Marashli¹, Ho Lai Henry Lam¹, Hamam Mokayed², Fredrik Sandin², Marcus Liwicki², Ho-Kin Tang³, Wing Chi Yu^{1*}

¹ Department of Physics, City University of Hong Kong, Kowloon, Hong Kong

² Department of Computer Science, Electrical and Space Engineering, Luleå University of Technology, 971 87 Luleå, Sweden

³ School of Science, Harbin Institute of Technology, Shenzhen, 518055, China

* wingcyu@cityu.edu.hk

Abstract

In this work, we proposed a novel approach for identifying quantum phase transitions in one-dimensional quantum many-body systems using AutoEncoder (AE), an unsupervised machine learning technique, with minimal prior knowledge. The training of the AEs is done with reduced density matrix (RDM) data obtained by Exact Diagonalization (ED) across the entire range of the driving parameter and thus no prior knowledge of the phase diagram is required. With this method, we successfully detect the phase transitions in a wide range of models with multiple phase transitions of different types, including the topological and the Berezinskii-Kosterlitz-Thouless transitions by tracking the changes in the reconstruction loss of the AE. The learned representation of the AE is used to characterize the physical phenomena underlying different quantum phases. Our methodology demonstrates a new approach to studying quantum phase transitions with minimal knowledge, small amount of needed data, and produces compressed representations of the quantum states.

1

2 Contents

3	1 Introduction	2
4	2 The machine learning model	3
5	3 Learning the Phase Diagrams	6
6	3.1 Spin-1/2 XXZ model	6
7	3.2 Spin-1 XXZ model	8
8	3.3 The Su-Schrieffer-Heeger Model	11
9	4 Conclusion	12
10	5 Acknowledgment	13
11	References	14
12	A iDMRG correlation length in the Spin-1/2 XXZ Model	18
13	B Data Preprocessing	18
14	C Entanglement Spectrum in the Spin-1 XXZ Model	19

D Classifier for phase prediction of the spin-1 XXZ model

19

1 Introduction

Understanding the quantum phases and phase transitions of quantum many-body systems is a fundamental problem in condensed matter physics. Different phases give rise to physical phenomena such as superconductivity and topological insulators [1] which can have a wide range of applications [2, 3]. Detecting and characterizing these transitions in quantum many-body systems is often challenging and requires extensive study of the systems or significant computational resources.

Traditional methods rely on the knowledge of the order parameters to detect phase transitions in quantum systems [4]. These order parameters serve as indicators of the system's state and its transitions between different phases. However, finding a suitable order parameter is a highly non-trivial task, especially in topological systems. In topological systems, the order parameter is usually non-local, meaning it cannot be described by local observables at a single point in the system. Instead, it often involves correlations between distant parts of the system, making its identification and measurement more challenging. Recent advancements in the study of topological phases have highlighted the importance of non-local string order parameters in capturing the unique properties of these systems [5].

Other popular approaches of detecting phase transitions involve measuring the entanglement [6–8] or the correlation length in the infinite Density Matrix Renormalization Group (iDMRG) [9]. These methods do not define an order parameter for the phase transition but attempt to provide information about how correlation changes in the system which often corresponds to a phase change. However, they can be model or phase specific and may not always work. The entanglement is not uniquely defined and there exists ambiguity in partitioning the system so that the entanglement measured can signal the transitions between different phases. The correlation length in iDMRG also does not always possess significant changes across phase transitions (see an example in Appendix A). Furthermore, the use of iDMRG requires translational symmetry and an area-law entanglement, which can limit its application in, for example, disorder systems or states of matters that are determined by long-time dynamics.

With machine learning (ML) techniques being developed to analyze large data systems, recent studies have shown they can be efficient tools for solving problems in natural sciences [10] such as biology [11, 12], chemistry [13] and physics [14] including identifying and characterizing quantum phases and phase transitions [15–19]. Early works such as Ref. [20] and Ref. [21] used supervised learning with binary classifier neural network to detect phase transition in the Ising model, and many-body localization mobility edge in the spin-1/2 Heisenberg chain in a random external field, respectively. These works demonstrated the viability of neural networks in detecting phase transitions in equilibrium and out-of-equilibrium systems. However, they had the limitations of needing labeled data, thus prior knowledge of the phase diagram, for supervised training and was only demonstrated for binary classification of a single transition.

Since then new unsupervised machine learning techniques have been introduced to detect phase transitions in a variety of models without the need of labeled data and without empirical knowledge of the order parameters [17–19]. Examples of promising recent works in this field are Chung *et al.* which used spin-spin correlation as input with Autoencoders (AE) and K-means clustering to find the transition points [17], and Han *et al.* which used Monte Carlo

61 state configurations as input for an unsupervised contrastive learning inspired by SimCLR ar-
62 chitecture [22] to find the phase transitions [18]. However, these works have some drawbacks
63 in limitation and requirements, for example in Chung *et al.* work the choice of the spin-spin
64 correlation functions for each system affects the results [17], making prior knowledge and
65 understanding of the system essential for accurately determining the transition points. While
66 in Han *et al.* work, up to 10^5 state configurations are required for each state in the driving pa-
67 rameter space [18], thus demanding significant computational power and limiting the ability
68 of exploring systems with multiple driving parameters.

69 On the other hand, Kottmann *et al.* used the entanglement spectrum as input and traced
70 the loss of an AE with symmetric connections trained on a single phase to obtain the phase dia-
71 gram of the one-dimensional (1D) extended Bose-Hubbard model [19]. The working principle
72 is similar to the fidelity approach which measures the similarity between two quantum states,
73 and the phase transitions are signaled by the minimum of the fidelity [23–26]. Here the AE loss
74 is the analogous to the similarity of the input data to the training region learned. The method
75 unveiled the novel region of phase separation between the supersolid and superfluid without
76 invoking the analysis of the order parameter and the energy gaps [27]. However, this method
77 is not fully unsupervised in the sense that brief knowledge of the phase diagram is needed in
78 advance to prepare the training samples. When applying the method on other condensed mat-
79 ter systems, we found that the results depend on the choice of the training region. Moreover,
80 some phase transitions do not show corresponding change with the entanglement spectrum
81 input, necessitating a different input capturing more information and better representation of
82 the quantum state.

83 In this work, we use the reduced density matrix (RDM) of a many-body system as a better
84 input to the AE to detect phase transitions. With fundamental modifications to the machine
85 architecture, we trained our machine with data expanding over the entire parameter space,
86 thus no prior knowledge of the phase diagram or the order parameter is required. Our scheme
87 successfully identified the rich phase diagram in a variety of one-dimensional models, includ-
88 ing the spin-1/2 XXZ model where the transition is of Berezinskii-Kosterlitz-Thouless (BKT)
89 type, the spin-1 XXZ model possessing the topological Haldane phase, and the spinless Su-
90 Schrieffer-Heeger model with interactions. Our approach requires no prior knowledge of the
91 model studied, nor specific training regions, and it works with small amount of training data
92 and on a variety of quantum many-body systems and different types of quantum phase tran-
93 sitions. We also demonstrated the learning ability of the AE by analysing the embedded layer
94 structure of the trained machine and showed that it learns a compressed representation of the
95 states that is distinct for different phases.

96 2 The machine learning model

97 The methodology employed in this study comprises three main stages and is summarized in
98 the flowchart shown in Fig. 1. In the first stage, data generation is executed using exact
99 diagonalization (ED) [28] implemented in the python package QuSpin [29, 30]. Despite ED
100 simulations are limited to small system size, this is balanced by its ease of implementation and
101 accuracy, making it a valuable technique that is used to study contemporary topics in many-
102 body systems [31, 32]. In addition, ED can simulate a wide range of non-equilibrium and
103 complex systems which can be difficult for other numerical methods. For example, in some
104 non-Hermitian systems, large-sized systems can be prone to numerical instabilities [33] that
105 may hinder the use of iDMRG for the study. The ED method provides us with a numerical
106 solution for the ground state $|\Psi_0(\lambda)\rangle$ of the many-body system at different driving parameters
107 λ with high accuracy. The system's half-block RDMs are then calculated by tracing out the

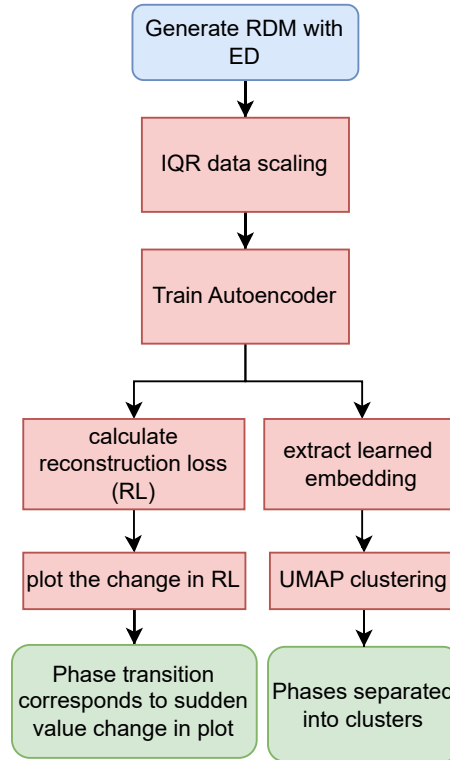


Figure 1: Flowchart illustrating the steps taken to identify quantum phase transitions in a quantum many-body system with a given Hamiltonian.

108 degrees of freedom outside the subsystem A , i.e. $\rho_A = \text{Tr}_{\notin A} |\Psi_0(\lambda)\rangle \langle \Psi_0(\lambda)|$, and are chosen as
 109 the input data since they are rich in information about the system and previous works have
 110 shown the capability of using the RDM to derive the potential order parameters of different
 111 quantum phases [34,35]. When simulating the input data, we increment the driving parameter
 112 with steps of order 0.01, generating about 200-800 data points for systems with a single driving
 113 parameter and 40,000-160,000 data points for systems with two driving parameters. The
 114 resulting RDM data is then subjected to a scaling process utilizing the interquartile range
 115 (IQR) robust scalar and simple clipping (see Appendix B). This scaling technique is used due
 116 to its resilience against outliers, thereby ensuring the data utilized is not skewed.

117 The second stage involves leveraging the AE, a neural network architecture designed for
 118 unsupervised learning. The AE consists of two primary components: an encoder, which maps
 119 the input to a lower-dimensional latent representation, and a decoder, which maps this lower-
 120 dimensional representation back to the original input space. The dimension of the latent space
 121 is usually set to be lower than that of the input to prevent the AE from trivially copying the
 122 input to the output. In this work, we use a deep learning model consisting of two layers of
 123 convolutional AE with a shortcut connection across the second layer as sketched in Fig. 2. The
 124 symmetric shortcut connection allows information to be passed directly from the encoder to
 125 the decoder, bypassing intermediate layers [36]. The feature maps from a shortcut connection
 126 and the connected deconvolutional layer are then added, allowing the network to combine
 127 information from multiple levels of abstraction.

128 One application of AE is anomaly detection, where the network is trained on a dataset
 129 containing mostly normal or non-anomalous data. The AE encodes and decodes this data,
 130 and the reconstruction error - the difference between the original input and the reconstructed
 131 output - is calculated. A small reconstruction error indicates that the input data is similar to the
 132 training data and is therefore considered as normal. Conversely, a large reconstruction error

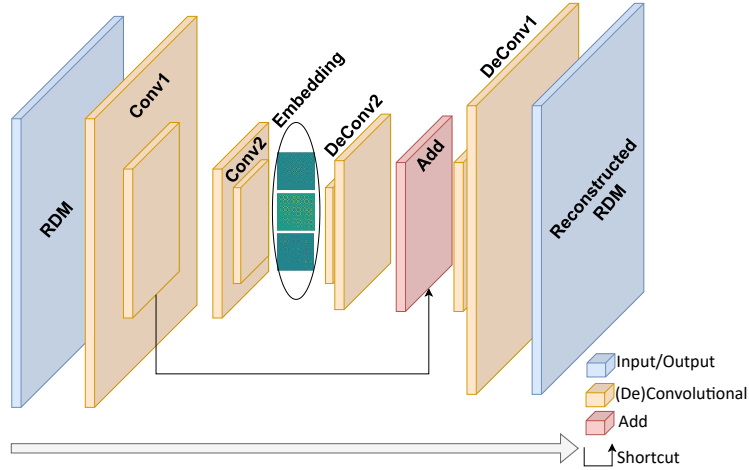


Figure 2: Schematic drawing of the RDM deep learning AE model architecture with shortcut connection.

133 suggests that the input data differs significantly from the training data and may be anomalous
 134 or abnormal. Identifying phase transition is analogous to anomaly detection since data at the
 135 transition boundary differs significantly from the data within a phase. Therefore, one may
 136 train the AE with data from a single phase and detect the transition from the abrupt increase
 137 in the reconstruction error [19]. However, such an approach still requires brief knowledge of
 138 the phase diagram to select the training data.

139 On the other hand, if an AE is trained on multiple distinct types of data, it may exhibit
 140 different reconstruction errors for each type. This is because the AE learning rate and com-
 141 pression loss of each data type can differ. Thus, an AE's reconstruction errors may vary for
 142 different types of data depending on how well it has learned their respective characteristics
 143 during training. This means we can train the AE on entire parameter space containing multiple
 144 phases while still being able to distinguish the different phases, achieving the truly unsuper-
 145 vised detection of phase transitions. In this work, we trained our AE across the entirety of
 146 the data range for single driving parameter systems and on about 10% of the data chosen
 147 randomly for systems with two driving parameters.

148 Finally, in the third stage, a visualization process is implemented. This is achieved by
 149 calculating the Mean Squared Error (MSE), which quantifies the loss between the original
 150 input and the AE's reconstruction, i.e.

$$\text{MSE}(A, B) = \frac{1}{n^2} \sum_{i=1}^n \sum_{j=1}^n (A_{ij} - B_{ij})^2, \quad (1)$$

151 where A and B is the $n \times n$ input and output matrix respectively. In the following, we will use
 152 MSE and AE loss interchangeably but they should be understood as the equation above. The
 153 rate of change of the AE loss as a function of the driving parameters is then plotted for analysis.
 154 It is postulated that changes in the gradient of this plot can be interpreted as corresponding to
 155 a phase transition within the system under study. This is because transition points can act as
 156 outliers in data, leading to an abrupt increase in the reconstruction error. Furthermore, differ-
 157 ent phases will be learned with different accuracy resulting in changes in loss. By observing
 158 these changes, we aim to identify the phase transitions in the systems being studied. In ad-
 159 dition, we also extracted the learned embedding representation of RDM at the Autoencoder
 160 bottleneck and clustered it according to the quantum phases.

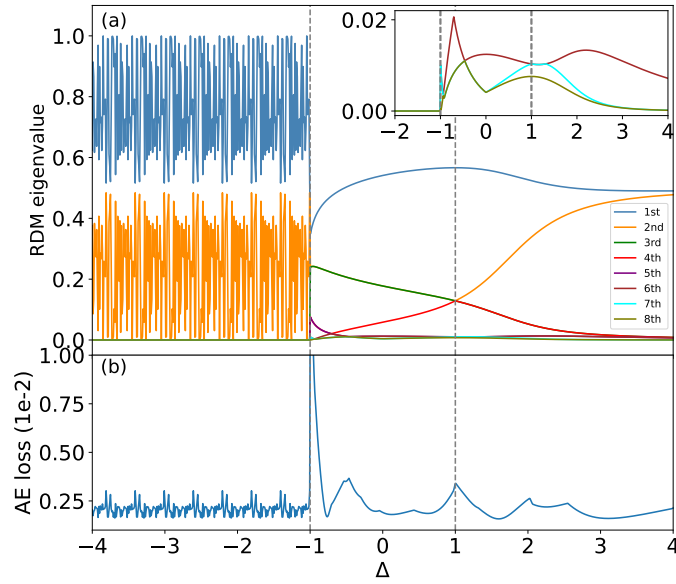


Figure 3: (a) The first eight eigenvalues of the half-block reduced density matrix of the spin-1/2 XXZ chain with $N = 20$ sites. Inset shows zoom-in of the 6th to 8th eigenvalues where spectrum crossing at $\Delta = -0.5$ and local maximum at $\Delta = 2$, which do not correspond to a phase transition, are observed. (b) The AE loss as a function of the driving parameter. There are peaks at Δ 's not corresponding to the transition points but as a result of the changes in the entanglement spectrum structure. The vertical dashed lines indicate the theoretically predicted critical points.

161 3 Learning the Phase Diagrams

162 We apply the above scheme to several 1D quantum systems, including spin and fermionic mod-
 163 els possessing various types of phase transitions. The periodic boundary condition is adopted
 164 unless otherwise specified. The results demonstrate the capability of our method in identifying
 165 different quantum phase transitions with high accuracy.

166 3.1 Spin-1/2 XXZ model

167 The Hamiltonian of the XXZ model reads

$$H = \sum_j (S_j^x S_{j+1}^x + S_j^y S_{j+1}^y + \Delta S_j^z S_{j+1}^z), \quad (2)$$

168 where S_j^x, S_j^y, S_j^z are the spin-1/2 operators and Δ is the parameter characterising the anisotropy
 169 in the spin-spin interaction. The ground state phase diagram consists of three distinct phases:
 170 the ferromagnetic (FM) phase, the critical (XY) phase, and the antiferromagnetic (AFM) phase
 171 [38–41]. The system experiences quantum phase transitions between these phases with the
 172 anisotropy parameter Δ at -1 and 1 respectively. The XY-AFM transition at $\Delta = 1$ is a Berezinskii-
 173 Kosterlitz-Thouless (BKT) type which have been challenging for detection using other methods
 174 such as the fidelity susceptibility [25, 42, 43].

175 In Kottman *et. al.*'s work, they mainly used the entanglement spectrum, i.e. the half-block
 176 reduced density matrix eigenvalues, from a single phase as training data for the AE [19].
 177 However, we find that the entanglement spectrum is insufficient and presents some issues
 178 when AE is trained on the entire parameter range as shown in figure 3(b). While there are
 179 peaks in the AE loss signalling the transitions at $\Delta = -1$ and 1 respectively, there are also other

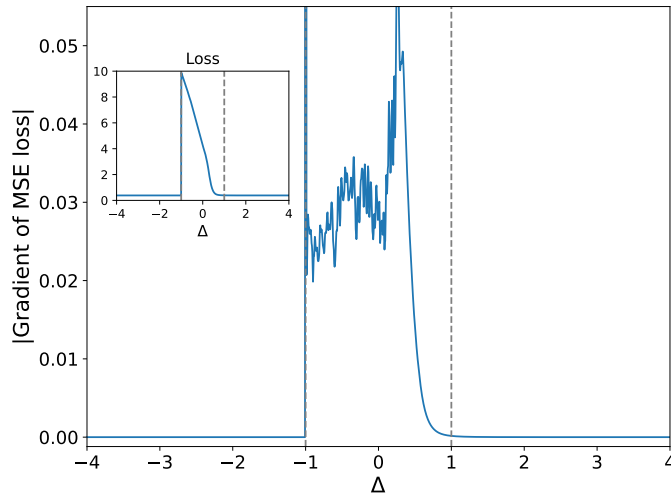


Figure 4: Magnitude of the gradient of the AE loss for the spin-1/2 XXZ model train on half-block RDM. Inset shows the AE loss as a function of Δ . Here $N = 20$. The vertical dashed lines correspond to the theoretical transition points at $\Delta = \pm 1$.

180 peaks with comparable magnitudes to the one at $\Delta = 1$ (the BKT transition) taking place
 181 within a phase. This can be understood from the qualitative structure of the entanglement
 182 spectrum, where the first eight values as a function of Δ are plotted in Fig. 3(a). The two
 183 peaks at $\Delta = -1$ and 1 reflect the significant changes in the two dominating eigenvalues in
 184 the spectrum. However, the lower eigenvalues can also carry non-trivial features, for example,
 185 the crossing around $\Delta = -0.5$ and the local maximum around $\Delta = 2$ without the system
 186 undergoing a phase transition. This in turn causes the additional peak observed in the AE
 187 loss.

188 This shows that using the entanglement spectrum to train on an entire parameter space
 189 requires prior knowledge of which eigenvalues to focus on. However, this will then defeat
 190 the goal of investigating phase transitions in new models. Even though the transitions in this
 191 spin-1/2 XXZ model have significant changes in the dominating eigenvalues, this may not be
 192 the case for other models. One example is the Spin-1 XXZ model which we considered in the
 193 next section (see Appendix C).

194 To solve the issue, we turn to training the AE with half-block RDM data from the entire
 195 range of Δ . The entanglement spectrum is derived from the eigenvalues of the RDM and offers
 196 insights into entanglement of the subsystem and its complement. The RDM, from which the
 197 entanglement spectrum is derived, provides a more comprehensive picture, encompassing a
 198 complete description of the subsystem's state including the entanglement information. This
 199 depth of information within the RDM can make discerning quantum phases difficult. However,
 200 with neural networks capabilities analyzing complex data, it becomes feasible to use RDM to
 201 identify phase transitions. As such, in our use of AE to detect phase transitions in quantum
 202 many-body systems, the RDM stands out as a more advantageous input compared to the en-
 203 tanglement spectrum. Figure 4 shows the resultant AE loss and its gradient magnitude as a
 204 function of Δ . There are three main distinctive regions corresponding to the three phases,
 205 and the transitions are captured by the abrupt changes in the loss gradient near $\Delta = -1$ and
 206 1. The FM and AFM phases have low AE loss and gradient. On the other hand, the XY phase
 207 starts with the highest loss but decreases in a linear like fashion with small fluctuations that
 208 plateaus at the XY-AFM transition point. This suggests learning the FM and AFM phases is
 209 easier than the XY phase, which is also consistent with the expectation that the XY phase has
 210 a more complex order parameter. Note that despite the similarity in concept between the AE

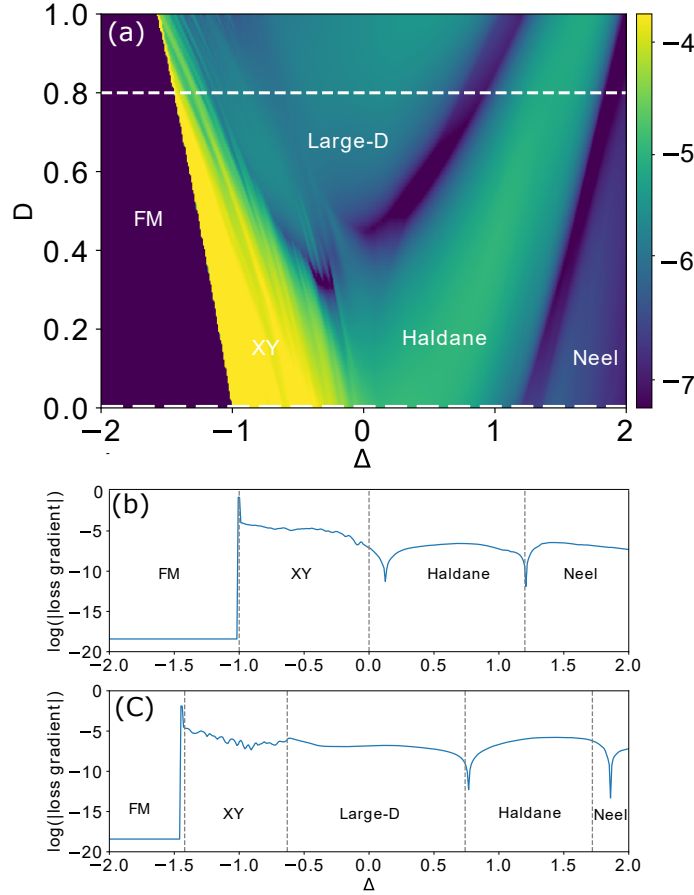


Figure 5: (a) The color map of the logarithm of the magnitude of AE loss gradient for the spin-1 XXZ model with Δ and D as the driving parameters. (b) and (c) shows the logarithm of the magnitude of AE loss gradient at fixed $D = 0$ and $D = 0.8$, respectively. The vertical dashed lines correspond to the transition points predicted in [37]. Lattice size of $N = 12$ is used here.

211 approach and the fidelity approach, we managed to detect the XY-AFM transition with GS data
 212 while the latter approach needed 1st excited state to detect the transition [26].

213 3.2 Spin-1 XXZ model

214 We next consider a system with more than one driving parameter. The one-dimensional Spin-1
 215 XXZ Model with uniaxial single-ion-type anisotropy given by the Hamiltonian [37]

$$H = \sum_j (S_j^x S_{j+1}^x + S_j^y S_{j+1}^y + \Delta S_j^z S_{j+1}^z) + D \sum_j (S_j^z)^2, \quad (3)$$

216 where S_j^x, S_j^y, S_j^z are the spin-1 operators at site j , Δ is the spin-spin interaction anisotropy
 217 parameter, and D characterises the uniaxial single-ion anisotropy. The system has a rich
 218 ground state phase diagram consisting of a topological Haldane phase, a large-D, Neel, FM
 219 and XY phases. The system undergoes quantum phase transitions between these phases as the
 220 anisotropy parameters Δ and D are varied.

221 Figure 5(a) shows the magnitude of the AE loss as a function of the driving parameters
 222 for the machines trained on RDM data. Given that our training data has increased by over an
 223 order of magnitude with two driving parameters, the AE's loss and its gradient are significantly

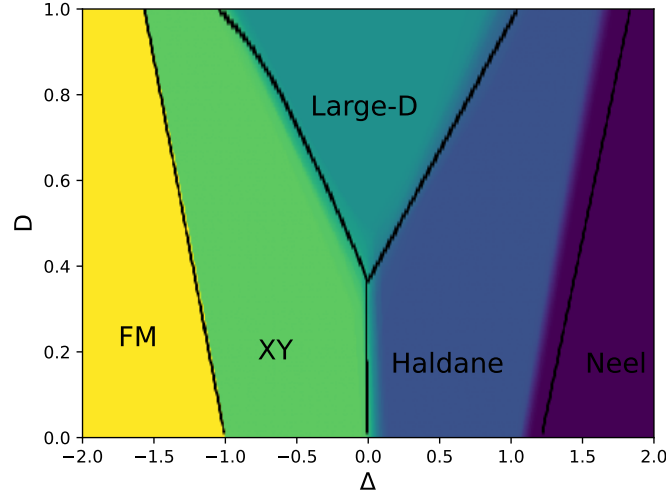


Figure 6: Classifier phase prediction of spin-1 XXZ model. Black lines represents the phase boundaries extracted from Ref. [37].

224 reduced. Therefore, we use a logarithmic scale when plotting to more clearly visualize these
 225 changes. Five distinct regions can be identified, among which the regions corresponding to
 226 the FM and XY phases are particularly prominent. Although the other regions have a close
 227 magnitude of the AE loss, clear boundaries separating these regions can be observed. In figures
 228 5(b) and (c), we extract the logarithmic changes in loss at fixed $D = 0$ and $D = 0.8$ respectively
 229 as a function of Δ . The sudden changes in loss gradient align closely with the predicted phase
 230 transition points in the literature [37]. This alignment underscores the reliability of the method
 231 in estimating the transition points.

232 To achieve clearer boundaries between the phases, especially between the XY, large-D and
 233 the Haldane phases, we trained 50 simple supervised classifier networks (with the architecture
 234 presented in Appendix D) on small regions (200 data points) centered within each phase as
 235 identified in Fig. 5, and used the networks to predict the phase diagram. The predicted phase
 236 diagram with the phase boundary averaged over the 50 runs is shown in Fig. 6, and the
 237 transition points for $D = 0$ and $D = 0.8$ are presented in Table 1. The obtained critical points
 238 match well with the expected results in Ref. [37] for transitions between the FM, XY, large-
 239 D, and Haldane phases, with a slight deviation in the Haldane-Neel transition. The slight
 240 deviation may attribute to the fact that the topological Haldane phase is more difficult to
 241 learn in general due to the long range entanglement and the classifier learned features of the
 242 Haldane phase near the Haldane-Neel transition are too similar to learned features of the Neel
 243 phase.

244 After training the AE on the RDM data, it learns a compressed representation in each
 245 layer. We examine the learned representation at the bottleneck, where the RDM size has been
 246 compressed from $3^6 \times 3^6 = 729 \times 729$ to 81×81 . Figure 7 shows visualizations of the learned
 247 representations picked from two points in each phase. The learned representations from each
 248 phase show a distinct pattern, indicating the AE's ability to learn distinct features for each
 249 phase.

D = 0		
Transition	Mean prediction \pm std	Expected
FM-XY	-1.01 ± 0.00	-1.00 ± 0.05
XY-Haldane	0.05 ± 0.04	0.00 ± 0.05
Haldane-Neel	1.10 ± 0.03	1.20 ± 0.05
D = 0.8		
Transition	Mean prediction \pm std	Expected
FM-XY	-1.45 ± 0.00	-1.50 ± 0.05
XY-LargeD	-0.67 ± 0.05	-0.60 ± 0.05
LargeD-Haldane	0.67 ± 0.08	0.70 ± 0.05
Haldane-Neel	1.54 ± 0.03	1.70 ± 0.05

Table 1: Comparison of predicted and expected transition points in the spin-1 XXZ model at different values of D . The error in the prediction is taken as the standard deviation, denoted as "std". The expected value is taken from digitizing Fig. 1 in Ref. [37] with an accuracy of 0.1.

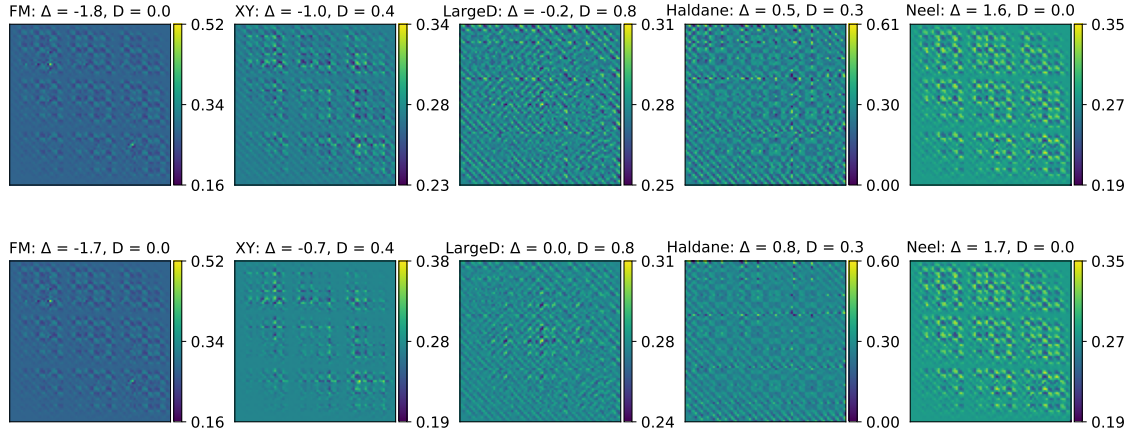


Figure 7: Learned bottleneck embedding of the five phases in spin-1 XXZ model. The rows show that embeddings are different when Δ, D are sampled from different phases, while the columns show that the embedding is similar when they are sampled from the same phase.

250 We further analysed the learned representations by projecting them into 2D feature space
 251 using a non-linear dimensionality reduction technique known as Uniform Manifold Approximation
 252 and Projection (UMAP) [44]. Dimensionality reduction is a process used in data analysis
 253 and machine learning to simplify high-dimensional data into a lower-dimensional form,
 254 making it more manageable and computationally efficient. By reducing the number of random
 255 variables under consideration, it retains the essential features of the data, thereby facilitating
 256 tasks such as data visualization. The UMAP stands out for its effectiveness and efficiency. It
 257 operates on the principle that uses Riemannian geometry to construct a graph representation
 258 of the high-dimensional data. The algorithm then optimizes a low-dimensional graph to
 259 closely resemble the high-dimensional one, resulting in a simplified representation that retains
 260 the original data's topological structure. By preserving the global structure of data, UMAP al-
 261 lows for the clear identification of clusters or groups of similar data points, providing valuable
 262 insights that are critical in data-driven decision-making processes.

263 We trained a UMAP transformer on 200 data points from each of the five phases observed

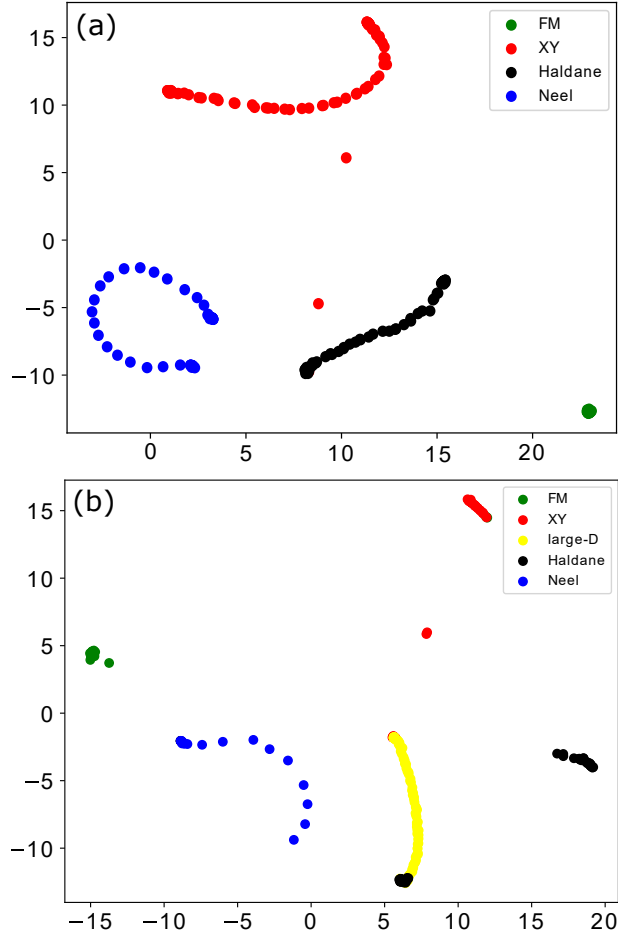


Figure 8: UMAP visualization of the AE learned representation for the spin-1 XXZ model RDM projected onto a 2D feature space. Here the lattice size is $N = 12$, $D = 0$ and 0.8 in (a) and (b) respectively, with $\Delta = [-2, 2]$. The data points are colored with respect to the expected transition points in Ref. [37].

264 in Fig. 5(a) and use it to visualize the learned representations in the AE on a 2D feature space.
 265 Figures 8 (a) and (b) show the visualization of the learned representation at $D = 0$ and 0.8
 266 respectively for $\Delta = [-2, 2]$, which is the same range shown in Figs. 5 (b) and (c) . It is
 267 clear that each phase data points cluster together forming four separate clusters, with few
 268 outliers at transition boundaries, e.g. transition points between XY-Haldane being outliers,
 269 this matches with the small deviation of the theoretical transition point at $\Delta = 0$ shown in
 270 Figs. 5 (b) and (c). Being able to successfully cluster the phases embedding demonstrates
 271 that the learned representation contains information that correlates to the phase properties
 272 which makes it potentially useful in future analysis of the phases' order parameters and other
 273 machine learning applications [45, 46].

274 3.3 The Su-Schrieffer-Heeger Model

275 We further applied the proposed method to a spinless fermion model, namely the Su-Schrieffer-
 276 Heeger (SSH) model, which is a foundational model that has been frequently investigated in
 277 the study of topological insulators [35, 47]. The interacting SSH model is characterized by the
 278 following Hamiltonian:

$$\begin{aligned}
H = & -t \sum_j \left[(1 + \eta) c_{j,A}^\dagger c_{j,B} + (1 - \eta) c_{j,B}^\dagger c_{j+1,A} + h.c. \right] \\
& + U \sum_j n_{j,A} n_{j,B} + V \sum_j n_{j,B} n_{j+1,A},
\end{aligned} \tag{4}$$

279 where $c_{j,A(B)}^\dagger$ and $c_{j,A(B)}$ are the creation and annihilation operators for a spinless fermion at
280 site A(B) in the unit cell j , respectively. The parameter t represents the hopping amplitude
281 between the nearest-neighboring sites and is taken to be 1 for convenience, η is the parameter
282 characterizing the anisotropy in the intercell and the intracell hopping, and U and V char-
283 acterize the strength of intracell and intercell interactions respectively, $n_{j,A(B)} = c_{j,A(B)}^\dagger c_{j,A(B)}$
284 is the number operator at site A(B) of the j -th unit cell. In the absence of interactions, the
285 SSH model exhibits a topological phase denoted as O_- for $\eta < 0$ where a quasi-local order
286 parameter has been identified by careful analysis of the RDM spectrum [35, 47]. A topological
287 phase transition takes place at $\eta = 0$ and the system transforms to a trivial phase denoted
288 as O_+ for $\eta > 0$ [48]. In the presence of interactions, the model exhibits a rich ground state
289 phase diagram consisting of multiple phases [35].

290 We study the model at $\eta = -0.6$ and the interaction range $U \in [1.0, 5.0]$ and $V \in [-4.0, 0]$
291 where the topological phase O_- , the trivial phase O_+ , and a charge density wave (CDW) phase
292 reside in. The logarithm of the magnitude of the AE loss gradient is shown in Fig. 9. Two
293 boundary lines representing the transitions between the three phases are clearly observed in
294 plot (a). These transition lines mostly agree with that found in previous works [35, 47]. In
295 Fig. 9(b), we plot the logarithmic change of the loss at fixed $U = 3$ as a function of V . Sharp
296 spikes are observed at values of V that are consistent with the transition points found in [35].
297 The results further demonstrate the generalizability of our method to identify phase transition
298 in many-body systems.

299 4 Conclusion

300 In this work, we have presented an approach for identifying and visualizing quantum phase
301 transitions with minimal prior knowledge using unsupervised machine learning techniques
302 that does not require labeled data and does not need specific regions to train on. Our method
303 is based on neural networks, which enable us to measure changes in the reduced density ma-
304 trix with driving parameters by analysing the reconstruction loss. We have demonstrated the
305 capability of our method in detecting various types of phase transitions, including topological
306 and BKT transitions, in several quantum systems. No prior knowledge of the order parameters
307 or the phase diagram is required in the process, and our method does not necessitate a large
308 amount of training data and is effective even with small system sizes. This makes the method
309 readily applicable for studying phase transitions in a wide range of novel quantum systems,
310 thus serves as a new tool that complements existing methods by providing new perspectives
311 and broadening the range of the quantum systems that can be explored.

312 In addition, we showed that relevant features of a phase can be extracted from the com-
313 pressed representation embedding of the Autoencoder, which can be clustered according to
314 the system's phase with dimensionality reduction techniques such as UMAP. This suggests how
315 quantum states are represented within neural networks and can be useful for further analysis
316 to extract insights into the underlying physics of each phase and may help identify the order
317 parameters.

318 Looking forward, the approach described here can be further refined and expanded to
319 tackle even more complex systems. For example, non-equilibrium systems such as the many-

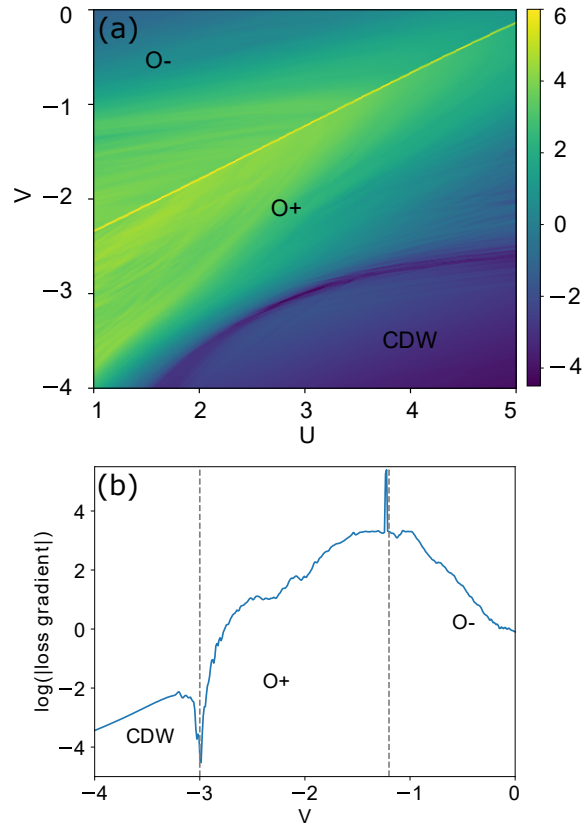


Figure 9: (a) Color map of the logarithm of the absolute AE loss gradient for the interacting SSH model with U and V as the driving parameters. (b) The logarithm of the absolute AE loss gradient as a function of V at fixed $U = 3$. Dashed lines at $V = -3, -1.2$ are the transition points obtained in [35]. Here $\eta = -0.6$ and a system size of 10 unit cells is considered.

320 body systems with disorders, periodically driven systems with non-equilibrium phases such as
 321 discrete time crystals [49, 50], or higher-dimensional systems.

322 5 Acknowledgment

323 We acknowledge financial support from Research Grants Council of Hong Kong (Grant No.
 324 CityU 11318722), National Natural Science Foundation of China (Grant No. 12204130), Shen-
 325 zhen Start-Up Research Funds (Grant No. HA11409065), City University of Hong Kong (Grant
 326 No. 9610438, 7005610, 9680320), and HITSZ Start-Up Funds (Grant No. X2022000).

327

328 **References**

- 329 [1] M. El-Batanouny, *Topological phases*, in *Advanced Quantum Condensed Matter Physics: One-Body, Many-Body, and Topological Perspectives* (Cambridge University Press, 2020),
330 pp. 217–218.
331
- 332 [2] I. Georgescu, S. Ashhab, and F. Nori, *Quantum simulation*, *Rev. Mod. Phys.* **86**, 153
333 (2014), doi:[10.1103/revmodphys.86.153](https://doi.org/10.1103/revmodphys.86.153).
- 334 [3] T. Wu, H. Mayaffre, S. Krämer, M. Horvatić, C. Berthier, W.N. Hardy, R. Liang, D.A. Bonn,
335 and M.-H. Julien, *Magnetic-field-induced charge-stripe order in the high-temperature su-
336 perconductor YBa₂Cu₃O_y*, *Nature* **477**, 191 (2011), doi:[10.1038/nature10345](https://doi.org/10.1038/nature10345).
- 337 [4] R. Arouca, A. Cappelli, and T.H. Hansson, *Quantum Field Theory Anoma-
338 lies in Condensed Matter Physics*, *SciPost Phys. Lect. Notes* **62** (2022),
339 doi:[10.21468/SciPostPhysLectNotes.62](https://doi.org/10.21468/SciPostPhysLectNotes.62).
- 340 [5] M. den Nijs and K. Rommelse, *Preroughening transitions in crystal surfaces and
341 valence-bond phases in quantum spin chains*, *Phys. Rev. B* **40**, 4709 (1989),
342 doi:[10.1103/PhysRevB.40.4709](https://doi.org/10.1103/PhysRevB.40.4709).
- 343 [6] A. Osterloh, L. Amico, G. Falci, and R. Fazio, *Scaling of Entanglement close to a Quantum
344 Phase Transition*, *Nature* **416**, 608 (2002).
- 345 [7] Y.C. Li, W.C. Yu, H.Q. Lin, *Detecting Quantum Phase Transitions in Spin Chains*, in *Entan-
346 glement in Spin Chains: Quantum Science and Technology*, edited by A. Bayat, S. Bose,
347 and H. Johannesson (Springer, 2022).
- 348 [8] T.J. Osborne and M.A. Nielsen, *Entanglement in a Simple Quantum Phase Transition*, *Phys.
349 Rev. A* **66**, 032110 (2002).
- 350 [9] R. Verresen, M.D. Lukin, and A. Vishwanath, *Prediction of toric code topological order from
351 Rydberg blockade*, *Phys. Rev. X* **11**, 031005 (2021), doi:[10.1103/PhysRevX.11.031005](https://doi.org/10.1103/PhysRevX.11.031005).
- 352 [10] G. Carleo, I. Cirac, K. Cranmer, L. Daudet, M. Schuld, N. Tishby, L. Vogt-Maranto, and
353 L. Zdeborová, *Machine learning and the physical sciences*, *Rev. Mod. Phys.* **91**, 045002
354 (2019), doi:[10.1103/revmodphys.91.045002](https://doi.org/10.1103/revmodphys.91.045002).
- 355 [11] W. Voon, Y.C. Hum, Y.K. Tee, W.-S. Yap, M.I.M. Salim, T.S. Tan, H. Mokayed, and K.W. Lai,
356 *Performance analysis of seven convolutional neural networks (CNNs) with transfer learning
357 for invasive ductal carcinoma (IDC) grading in breast histopathological images*, *Sci. Rep.*
358 **12**, 19200 (2022), doi:[10.1038/s41598-022-21848-3](https://doi.org/10.1038/s41598-022-21848-3).
- 359 [12] A.N.A. Masri and H. Mokayed, *An efficient machine learning based cervical cancer detection
360 and classification*, *J. Cyber Secur.* **2**, 58 (2020), doi:[10.54216/jcim.020203](https://doi.org/10.54216/jcim.020203).
- 361 [13] A. Gao and R.C. Remsing, *Self-consistent determination of long-range electrostatics in neu-
362 ral network potentials*, *Nat. Commun.* **13**, 1572 (2022), doi:[10.1038/s41467-022-29243-
363 2](https://doi.org/10.1038/s41467-022-29243-2).
- 364 [14] J. Carrasquilla, *Machine learning for quantum matter*, *Adv. in Phys.: X* **5**, 1797528 (2020),
365 doi:[10.1080/23746149.2020.1797528](https://doi.org/10.1080/23746149.2020.1797528).

- 366 [15] R.A. Vargas-Hernández, J. Sous, M. Berciu, and R.V. Krems, *Extrapolating*
367 *quantum observables with machine learning: Inferring multiple phase transi-*
368 *tions from properties of a single phase*, Phys. Rev. Lett. **121**, 255702 (2018),
369 doi:[10.1103/PhysRevLett.121.255702](https://doi.org/10.1103/PhysRevLett.121.255702).
- 370 [16] W. Hu, R.R.P. Singh, and R.T. Scalettar, *Discovering phases, phase transitions, and*
371 *crossovers through unsupervised machine learning: A critical examination*, Phys. Rev. E
372 **95**, 062122 (2017), doi:[10.1103/PhysRevE.95.062122](https://doi.org/10.1103/PhysRevE.95.062122).
- 373 [17] M.-C. Chung, G.-Y. Huang, I.P. McCulloch, and Y.-H. Tsai, *Deep learning of phase transi-*
374 *tions for quantum spin chains from correlation aspects*, Phys. Rev. B **107**, 214451 (2023),
375 doi:[10.1103/physrevb.107.214451](https://doi.org/10.1103/physrevb.107.214451).
- 376 [18] X.-Q. Han, S.-S. Xu, Z. Feng, R.-Q. He, and Z.-Y. Lu, *Framework for contrastive learning*
377 *phases of matter based on visual representations*, Chin. Phys. Lett. **40**, 027501 (2023),
378 doi:[10.1088/0256-307x/40/2/027501](https://doi.org/10.1088/0256-307x/40/2/027501).
- 379 [19] K. Kottmann, P. Huembeli, M. Lewenstein, and A. Acín, *Unsupervised phase*
380 *discovery with deep anomaly detection*, Phys. Rev. Lett. **125**, 170603 (2020),
381 doi:[10.1103/physrevlett.125.170603](https://doi.org/10.1103/physrevlett.125.170603).
- 382 [20] J. Carrasquilla and R.G. Melko, *Machine Learning Phases of Matter*, Nat. Phys. **13**, 431
383 (2017).
- 384 [21] F. Schindler, N. Regnault, and T. Neupert, *Probing many-body localization with neural*
385 *networks*, Phys. Rev. B **95**, 245134 (2017), doi:[10.1103/PhysRevB.95.245134](https://doi.org/10.1103/PhysRevB.95.245134).
- 386 [22] T. Chen, S. Kornblith, M. Norouzi, and G. Hinton, *A simple framework for contrastive*
387 *learning of visual representations*, in Proceedings of the 37th International Conference on
388 Machine Learning, edited by H.D. III and A. Singh (PMLR, 2020), Vol. 119, pp. 1597–
389 1607.
- 390 [23] P. Zanardi and N. Paunković, *Ground state overlap and quantum phase transitions*, Phys.
391 Rev. E **74**, 031123 (2006), doi:[10.1103/PhysRevE.74.031123](https://doi.org/10.1103/PhysRevE.74.031123).
- 392 [24] H.T. Quan, Z. Song, X.F. Liu, P. Zanardi, and C.P. Sun, *Decay of loschmidt*
393 *echo enhanced by quantum criticality*, Phys. Rev. Lett. **96**, 140604 (2006),
394 doi:[10.1103/PhysRevLett.96.140604](https://doi.org/10.1103/PhysRevLett.96.140604).
- 395 [25] S.-J. Gu, *Fidelity Approach to Quantum Phase Transitions*, Int. J. Mod. Phys. B **24**, 4371
396 (2010), doi:[10.1142/s0217979210056335](https://doi.org/10.1142/s0217979210056335).
- 397 [26] H.-K. Tang, M.A. Marashli, and W.C. Yu, *Unveiling quantum phase transitions by fidelity*
398 *mapping*, Phys. Rev. B **104**, 075142 (2021), doi:[10.1103/physrevb.104.075142](https://doi.org/10.1103/physrevb.104.075142).
- 399 [27] G.G. Batrouni, V.G. Rousseau, R.T. Scalettar, and B. Grémaud, *Competing phases, phase*
400 *separation, and coexistence in the extended one-dimensional bosonic Hubbard model*, Phys.
401 Rev. B **90**, 205123 (2014), doi:[10.1103/PhysRevB.90.205123](https://doi.org/10.1103/PhysRevB.90.205123).
- 402 [28] A.W. Sandvik, A. Avella, and F. Mancini, *Computational studies of quantum spin systems*,
403 in AIP Conference Proceedings (AIP, 2010), p. 135–338, doi:[10.1063/1.3518900](https://doi.org/10.1063/1.3518900).
- 404 [29] P. Weinberg and M. Bukov, *Quspin: a python package for dynamics and exact diagonali-*
405 *sation of quantum many body systems part i: spin chains*, SciPost Phys. **2**, 003 (2017),
406 doi:[10.21468/SciPostPhys.2.1.003](https://doi.org/10.21468/SciPostPhys.2.1.003).

- 407 [30] P. Weinberg and M. Bukov, *QuSpin: a Python package for dynamics and exact diagonalization of quantum many body systems. Part II: bosons, fermions and higher spins*, SciPost Phys. **7**, 020 (2019), doi:[10.21468/SciPostPhys.7.2.020](https://doi.org/10.21468/SciPostPhys.7.2.020).
- 410 [31] K. Sanada, Y. Miao, and H. Katsura, *Quantum many-body scars in spin models with multi-body interactions*, Phys. Rev. B **108**, 155102 (2023), doi:[10.1103/PhysRevB.108.155102](https://doi.org/10.1103/PhysRevB.108.155102).
- 412 [32] C. Chen et al., *Role of electron-phonon coupling in excitonic insulator candidate Ta_2NiSe_5* , Phys. Rev. Res. **5**, 043089 (2023), doi:[10.1103/PhysRevResearch.5.043089](https://doi.org/10.1103/PhysRevResearch.5.043089).
- 414 [33] E. Edvardsson and E. Ardonne, *Sensitivity of non-hermitian systems*, Phys. Rev. B **106**, 115107 (2022), doi:[10.1103/PhysRevB.106.115107](https://doi.org/10.1103/PhysRevB.106.115107).
- 416 [34] S.-J. Gu, W.C. Yu, and H.-Q. Lin, *Construct order parameters from the reduced density matrix spectra*, Ann. Phys. **336**, 118 (2013), doi:[10.1016/j.aop.2013.05.014](https://doi.org/10.1016/j.aop.2013.05.014).
- 418 [35] W.C. Yu, Y.C. Li, P.D. Sacramento, and H.-Q. Lin, *Reduced density matrix and order parameters of a topological insulator*, Phys. Rev. B **94**, 245123 (2016), doi:[10.1103/PhysRevB.94.245123](https://doi.org/10.1103/PhysRevB.94.245123).
- 421 [36] L.-F. Dong, Y.-Z. Gan, X.-L. Mao, Y.-B. Yang, and C. Shen, *Learning deep representations using convolutional auto-encoders with symmetric skip connections*, in Proceedings of the IEEE International Conference on Acoustics, Speech and Signal Processing (ICASSP), 2018, pp. 3006–3010, doi:[10.1109/icassp.2018.8462085](https://doi.org/10.1109/icassp.2018.8462085).
- 425 [37] W. Chen, K. Hida, and B.C. Sanctuary, *Ground-state phase diagram of $s=1$ XXZ chains with uniaxial single-ion-type anisotropy*, Phys. Rev. B **67**, 104401 (2003), doi:[10.1103/PhysRevB.67.104401](https://doi.org/10.1103/PhysRevB.67.104401).
- 428 [38] M. Kargarian, R. Jafari, and A. Langari, *Renormalization of entanglement in the anisotropic heisenberg (XXZ) model*, Phys. Rev. A **77**, 032346 (2008), doi:[10.1103/PhysRevA.77.032346](https://doi.org/10.1103/PhysRevA.77.032346).
- 431 [39] S.S. Rahaman, S. Haldar, and M. Kumar, *Machine learning approach to study quantum phase transitions of a frustrated one dimensional spin-1/2 system*, J. Phys.: Condens. Matter **35**, 115603 (2023), doi:[10.1088/1361-648x/acb030](https://doi.org/10.1088/1361-648x/acb030).
- 434 [40] Y. Yao, H.-W. Li, C.-M. Zhang, Z.-Q. Yin, W. Chen, G.-C. Guo, and Z.-F. Han, *Performance of various correlation measures in quantum phase transitions using the quantum renormalization-group method*, Phys. Rev. A **86**, 042102 (2012), doi:[10.1103/PhysRevA.86.042102](https://doi.org/10.1103/PhysRevA.86.042102).
- 438 [41] V. Alba, B. Bertini, M. Fagotti, L. Piroli, and P. Ruggiero, *Generalized-hydrodynamic approach to inhomogeneous quenches: correlations, entanglement and quantum effects*, J. Stat. Mech. **2021**, 114004 (2021), doi:[10.1088/1742-5468/ac257d](https://doi.org/10.1088/1742-5468/ac257d).
- 441 [42] S.-J. Gu, H.-M. Kwok, W.-Q. Ning, and H.-Q. Lin, *Fidelity susceptibility, scaling, and universality in quantum critical phenomena*, Phys. Rev. B **77**, 245109 (2008), doi:[10.1103/PhysRevB.77.245109](https://doi.org/10.1103/PhysRevB.77.245109).
- 444 [43] S.-J. Gu and W.C. Yu, *Spectral function and fidelity susceptibility in quantum critical phenomena*, EPL **108**, 20002 (2014), doi:[10.1209/0295-5075/108/20002](https://doi.org/10.1209/0295-5075/108/20002).
- 446 [44] L. McInnes, J. Healy, N. Saul, and L. Großberger, *Umap: Uniform manifold approximation and projection*, J. Open Source Softw. **3**, 861 (2018), doi:[10.21105/joss.00861](https://doi.org/10.21105/joss.00861).

- 448 [45] K. Ch'ng, J. Carrasquilla, R.G. Melko, and E. Khatami, *Machine learning phases of strongly*
449 *correlated fermions*, Phys. Rev. X **7**, 031038 (2017), doi:[10.1103/physrevx.7.031038](https://doi.org/10.1103/physrevx.7.031038).
- 450 [46] X.-D. Bai, J. Zhao, Y.-Y. Han, J.-C. Zhao, and J.-G. Wang, *Learning single-particle mobility*
451 *edges by a neural network based on data compression*, Phys. Rev. B **103**, 134203 (2021),
452 doi:[10.1103/PhysRevB.103.134203](https://doi.org/10.1103/PhysRevB.103.134203).
- 453 [47] W.C. Yu, P.D. Sacramento, Y.C. Li, and H.-Q. Lin, *Correlations and dynamical quantum*
454 *phase transitions in an interacting topological insulator*, Phys. Rev. B **104**, 085104 (2021),
455 doi:[10.1103/PhysRevB.104.085104](https://doi.org/10.1103/PhysRevB.104.085104).
- 456 [48] W.P. Su, J.R. Schrieffer, and A.J. Heeger, *Solitons in polyacetylene*, Phys. Rev. Lett. **42**,
457 1698 (1979), doi:[10.1103/PhysRevLett.42.1698](https://doi.org/10.1103/PhysRevLett.42.1698).
- 458 [49] M.P. Zaletel, M. Lukin, C. Monroe, C. Nayak, F. Wilczek, and N.Y. Yao, *Colloquium:*
459 *Quantum and classical discrete time crystals*, Rev. Mod. Phys. **95**, 031001 (2023),
460 doi:[10.1103/RevModPhys.95.031001](https://doi.org/10.1103/RevModPhys.95.031001).
- 461 [50] W.C. Yu, J. Tangpanitanon, A.W. Glaetzle, D. Jaksch, and D.G. Angelakis, *Discrete time*
462 *crystal in globally driven interacting quantum systems without disorder*, Phys. Rev. A **99**,
463 033618 (2019), doi:[10.1103/PhysRevA.99.033618](https://doi.org/10.1103/PhysRevA.99.033618).

464 A iDMRG correlation length in the Spin-1/2 XXZ Model

465 Figure 10 compares the change in the gradient of AE loss with the correlation length obtained
 466 from iDMRG for spin-1 XXZ model in Eq. (3). Both methods accurately detect the topological
 467 to non-topological Haldane-Neel transition at $\Delta = 1.2$. However, the XY-Haldane transition,
 468 which is believed to be a BKT type, is not detected by the correlation length at $\Delta = 0$. In
 469 contrast, our method is able to capture this transition. This demonstrates an example of model
 470 specificity for iDMRG correlation length application and our method's potential for broader
 471 applicability across different quantum systems.

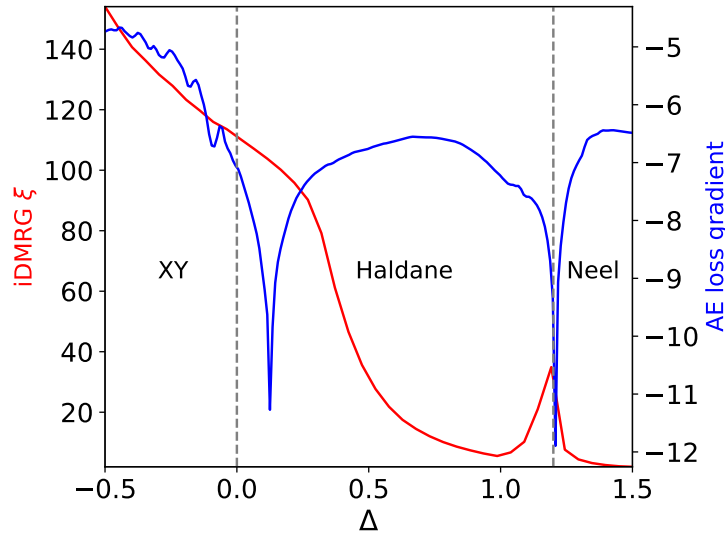


Figure 10: The gradient of AE loss (in blue) and iDMRG correlation length ξ (in red) as a function of the spin-spin interaction anisotropy parameter Δ in Spin-1 XXZ model. The uniaxial single-ion anisotropy is set to $D = 0$. A system of 12 sites is considered in the ED simulation in the AE approach. The theoretical phase transitions are indicated by the vertical dashed lines.

472 B Data Preprocessing

473 Data preprocessing is a crucial step in preparing data for machine learning algorithms and can
 474 significantly impact the performance of the model. One essential aspect of data preprocessing
 475 is data scaling, which involves normalizing data to a common range to prevent variables with
 476 large ranges from dominating the model. While standard scaling techniques such as z-score
 477 normalization and min-max scaling are commonly used, they may not be robust to outliers,
 478 which can significantly impact model performance and can change data spread (min-max scal-
 479 ing compress data inliers into a narrow range) and data distribution (standard scalar assumes
 480 normal distribution of data). In contrast, interquartile range (IQR) robust scaling, as defined
 481 by

$$X_{\text{scaled}} = \frac{X - \text{median}(X)}{\text{IQR}(X)}, \quad (5)$$

482 is a technique that can be used to normalize data in the presence of outliers. IQR robust scaling
 483 is based on the interquartile range of the data, which is less sensitive to outliers than the
 484 mean or standard deviation. We found that IQR followed by clipping outlier values is the best

485 performing scaling technique because the magnitude of the RDM values differs significantly
 486 across different phases and we need to scale the data such that all data is of similar order of
 487 magnitude. After the IQR robust scaling, we implement additional simple clip scaling to the
 488 99.9 percentile of the data to further reduce the influence of outlier points.

489 C Entanglement Spectrum in the Spin-1 XXZ Model

490 Figures 11 (a) and (b) show the first few values of the entanglement spectrum of the Spin-1
 491 XXZ. The first three dominating values of the spectrum are featureless at the transition be-
 492 tween XY-Haldane phases at $\Delta = 0$. The transition can be only observed starting from the
 493 4th eigenvalue where there is a level crossing. However, besides the features observed at the
 494 true critical points, lower eigenvalues also show non-trivial changes at $\Delta = -0.8$ and $\Delta = 1$
 495 which do not correspond to a phase transition. This will in turn lead to extra peaks in AE loss
 496 when it is trained with entanglement spectrum data as shown in figure 11 (c). This further
 497 demonstrates the deficiency of using ES as input for the AE.

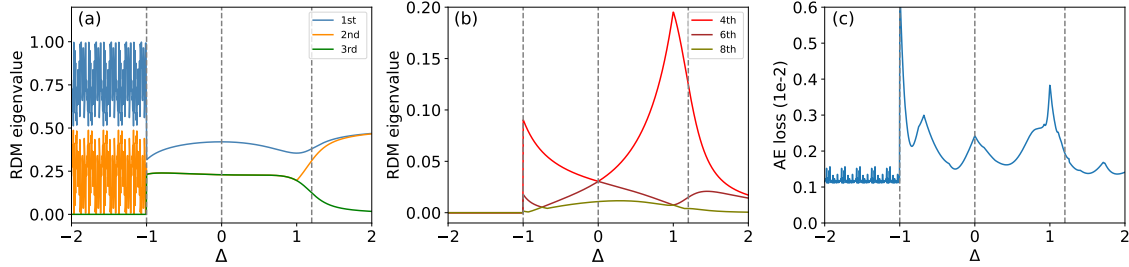


Figure 11: (a) The largest three eigen-values of the half-block RDM of the spin-1 XXZ model of lattice size $N = 12, D = 0$. The values change significantly near the FM-XY transition and the Haldane-Neel transition at $\Delta = -1$ and 1.2 respectively, but not the XY-Haldane transition point at $\Delta = 0$. (b) The 4th, 6th, 8th values of the entanglement spectrum. They show significant features at $\Delta = -0.8$ and 1 which do not correspond to any phase transitions. (c) Loss of AE trained on the entanglement spectrum. Vertical dashed lines indicate the theoretical transition points.

498 D Classifier for phase prediction of the spin-1 XXZ model

499 Figure 12 and Table 2 shows the schematic drawing and the detailed architecture of the net-
 500 work used for phase classification in the spin-1 XXZ model. The architecture is composed of
 501 two convolutional layers with strides and kernel size 3×3 followed by flatten and two dense
 502 layers with final softmax prediction layer that gives probability of each phase. Dropout of 20%
 503 is used between dense layers to prevent overfitting.

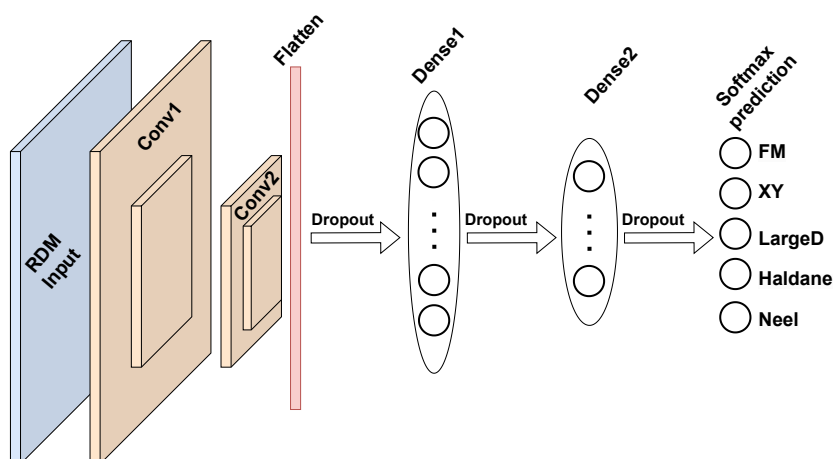


Figure 12: Schematic drawing of the RDM convolutional classifier model architecture.

Layer Number	Layer Type
1	Input
2	Conv2D + pooling
3	Conv2D + pooling
4	Flatten
5	Dropout
6	Dense
7	Dropout
8	Dense
9	Dropout
10	Dense (Softmax)

Table 2: Classifier model architecture